International Journal of Multiphase Flow 61 (2014) 1–13

Contents lists available at ScienceDirect

International Journal of Multiphase Flow

journal homepage: www.elsevier.com/locate/ijmulflow

Unsteady effects in dense, high speed, particle laden flows

J.D. Regele [a,*], J. Rabinovitch [b], T. Colonius [c], G. Blanquart [c]

[a] Aerospace Engineering, Iowa State University, Ames, IA 50011, USA
[b] Graduate Aerospace Laboratories, California Institute of Technology, Pasadena, CA 91125, USA
[c] Mechanical Engineering, California Institute of Technology, Pasadena, CA 91125, USA

ARTICLE INFO

Article history:
Received 9 May 2013
Received in revised form 24 December 2013
Accepted 29 December 2013
Available online 9 January 2014

Keywords:
Dense particle cloud
Shock wave
Particle laden
Drag coefficient

ABSTRACT

Dense high speed non-compacted multiphase flows exist in variable phase turbines, explosions, and ejector nozzles, where the particle volume fraction is in the range $0.001 < \alpha_d < 0.5$. A canonical problem that can be used to study modeling issues related to these types of flows is a shock wave impacting a planar particle cloud. Thus far, prior work has modeled the flow using a 1-D volume-averaged point particle approach and developed momentum and energy coupling terms that reproduce accurately the trajectory of particles in the experiments. Although these early results are promising, it is appropriate to question whether all aspects of the experimental flow can be captured using a one-dimensional model that is traditionally only used for dilute flows. Thus the objective of this work is to set-up a two-dimensional configuration that captures qualitatively the multidimensional behavior of a real three-dimensional particle cloud, but can be used as an exact solution to compare with an equivalent volume-averaged model. The 2-D data is phase-averaged to reduce it to one dimension, and x–t diagrams are used to characterize the flow behavior. These results show the importance of the Reynolds stress term inside the particle cloud and in its turbulent wake. A one-dimensional (1-D) model is developed for direct comparison with the 2-D simulation. While the 1-D model characterizes the overall steady-state flow behavior well, it fails to capture aspects of the unsteady behavior inside and behind the particle cloud because it neglects important unclosed terms.

1. Introduction

Dense high speed multiphase flows can be found in a variety of practical applications such as variable phase turbines, explosions, liquid rocket motors, and ejectors. In these applications, particles can be spaced far apart or close together. The range of scales encompassed by these applications precludes direct numerical simulation in the design process. Thus, sub-grid scale models are necessary in order to model these flows at practical scales.

There are different regimes of multiphase flow based on the disperse phase volume fraction α_d. In the dilute regime $\alpha_d \ll 1$, there are no collisions because the particles are far apart and the particles do not interact with each other. In the limit of the granular regime $\alpha_d \sim 1$, the particles are in constant contact with each other; their motion is controlled primarily by particle collisions, with small contributions from the continuous phase. The regime of interest in this paper is the dense non-granular regime ($0.001 < \alpha_d < 0.5$) between these two limiting extremes (Zhang et al., 2001).

Experiments and simulations used to study these regimes often rely on an initial shock wave to set up a high-speed flow through a particle cloud. In the dilute regime, these flows are well characterized (Carrier, 1958; Miura and Glass, 1982, 1983; Miura, 1990; Saito, 2002). Similarly, in the granular regime where the particles are densely packed, continuum mixture theories exist to describe these flows (Baer and Nunziato, 1986; Powers et al., 1990). However, little information exists for particle flow interactions where the volume fraction is in the range $0.001 < \alpha_d < 0.5$. Recently, a multiphase shock tube experiment has been developed at Sandia National Labs (Wagner et al., 2011, 2012) to explore dense high speed particle-laden flow. This experiment improves upon other configurations by isolating the dense non-compacted regime with a gravity fed curtain of nearly constant volume fraction in the stream-wise direction.

In the dilute regime, for both low Mach number (incompressible) and compressible flows, volume-averaged models combined with a point-particle approach have been used successfully to model multiphase flows (Clemins, 1988; Drew, 1983; Drew and Passman, 1999; Magnaudet and Eames, 2000; Crowe et al., 2012). These models rely on the assumption that the particle diameters are much smaller than the inter-particle distance. Under these conditions, the particles interact with the continuous phases independent from other particles and the coupling terms between the

* Corresponding author. Tel.: +1 515 294 1614; fax: +1 515 294 3262.
E-mail addresses: jregele@iastate.edu (J.D. Regele), jason.rabinovitch@caltech.edu (J. Rabinovitch), colonius@caltech.edu (T. Colonius), g.blanquart@caltech.edu (G. Blanquart).

0301-9322/$ - see front matter © 2014 Elsevier Ltd. All rights reserved.
http://dx.doi.org/10.1016/j.ijmultiphaseflow.2013.12.007

continuum and disperse phases can be modeled as independent single particle interactions (Crowe et al., 2012).

The point-particle approach, which assumes the individual particles are independent, is not valid for the granular regime where the flow is collision dominated. In other words, granular flow may not be modeled using information for only a single particle. However, in the dense non-compacted regime ($\alpha_d < 0.5$), this distinction is not so clear because the collisions are less frequent and the continuous phase contributes significantly to the particle dynamics. Simultaneously, the particles are sufficiently far apart that their effect on the continuum phase *might be* represented accurately enough using the same source terms as for the dilute regime.

Recently Ling et al. (2012) combines the experimental data of Wagner et al. (2012) with a one-dimensional volume-averaged point-particle model including unsteady momentum coupling forces. The leading and trailing edges of the particle cloud and transmitted and reflected shock locations predicted by the numerical model accurately match the experimental data. This was done by incorporating correction functions for finite particle Mach number and volume fraction. The correction function for Mach number is developed for a single sphere (Parmar et al., 2010) and the correction function for finite volume fraction is developed assuming the fluid has only minor acoustic waves (Sangani et al., 1991). In the current work, it will be demonstrated that volume-averaged models can reproduce accurately the reflected and transmitted shock locations, but that this approach incorrectly accounts for the large amount of energy that is contained in turbulent structures.

The goal of the present paper is to investigate the interactions between disperse and continuum phases in the dense non-compacted regime. More specifically, the objectives are threefold: (1) assess the validity of the volume-averaged models combined with a point-particle approach to model compressible multiphase flows; (2) identify the limitations/shortcomings of this technique; and (3) propose modifications to this approach that will better capture the physical phenomena that occur in these types of flows. To streamline the discussion, we ignore heat and mass transfer so that the results are restricted to a disperse phase of solid, adiabatic particles.

Towards this goal, the canonical problem of a shock wave impacting a planar particle cloud is considered. This configuration is intended to mimic the physics encountered in the aforementioned investigation of Wagner et al. (2012): namely compressible flow, dense non-compacted disperse phase, and nearly planar configuration (on average). While the coupling between the two phases is in reality two-way, the present work focuses only on the early stages of the experiments where the particles can be assumed, with good accuracy, to remain fixed in space. This should be considered as a necessary first step towards understanding the physics of the fluid-particle interaction.

The paper is organized as follows. In the following section, a 2-D configuration is presented that will model a planar shock wave impacting a particle cloud alongside the numerical framework used to solve the governing equations. Then, in Section 3, the numerical results of the 2-D simulations are presented. In Section 4, the phase-averaged equations for the present configuration are re-derived and commonly made assumptions are summarized and discussed. Finally, in Section 5, the solution of the 1-D phase-averaged equations are compared with the phase-averaged results of the 2-D exact flow field.

2. Detailed simulation of shock-particle interaction

In this section, a numerical simulation that captures the fluid-particle interactions for a dense multiphase flow is developed.

2.1. Assumptions

In the experiment of Wagner et al. (2012), the Reynolds number based on the velocity behind the reflected shock and the particle diameter is approximately $Re \approx 2000$. At this Reynolds number, the drag coefficient of a single individual particle is nearly constant and the flow is considered to be in the inertial range (Clift et al., 1978). Within the inertial range, viscous forces on the particles are negligible, and the drag force on a particle is predominantly from pressure drag. Nevertheless, it is important to note that molecular viscosity (albeit very small) is the reason for the separation of the boundary layer, which is why the drag coefficient is constant. In the present work, the Euler equations are used to model the flow through the particle cloud. As will be shown later, the artificial viscosity associated with the numerical discretization is sufficient to induce boundary layer separation and a realistic flow around the particles.

A two-dimensional simulation will be used to characterize the flow behavior. Although true multiphase flow is three-dimensional, two-dimensional simulations are an efficient first step in extracting the qualitative physical behavior. The flow around a sphere (3-D) and a cylinder (2-D), particularly the boundary layer separation point and transition Reynolds numbers, is different. However, the 2-D simulations are sufficient to investigate the fundamental differences between direct simulation and a volume-averaged point-particle model. A full three-dimensional demonstration will be the subject of future work.

The final major assumption in this work is that the particles have infinite inertia and can be considered frozen in place. While this assumption is perfectly valid for the objectives of this work, this limits the comparison that can be made with the experimental data (Wagner et al., 2012). Fig. 1 shows three different Schlieren

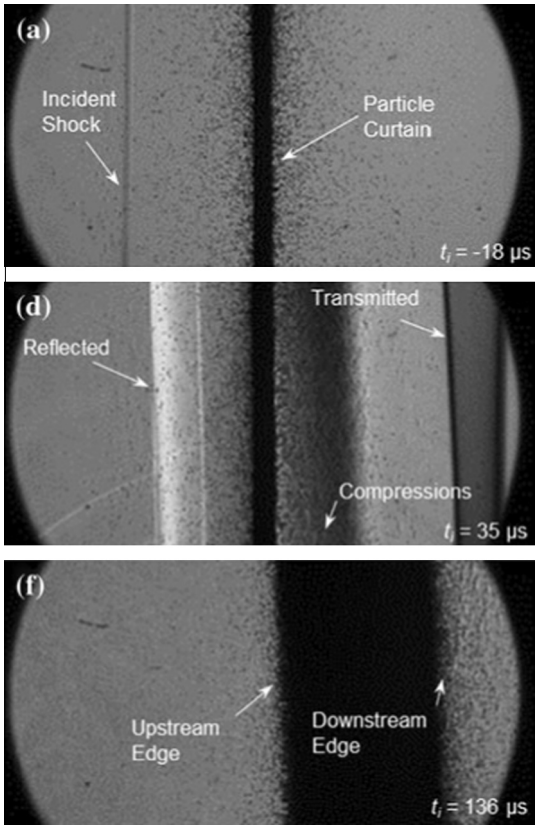

Fig. 1. Selected Schlieren images at times −18, 35, and 136 μs from Wagner et al. (2012).

images from Fig. 8 of Wagner et al. (2012). The first is 18 μs before the shock wave impacts the particle curtain, the second is 35 μs after the shock wave has impacted the curtain, and the third is 136 μs after shock wave impact. Little movement of the particle cloud is observed during the first 35 μs, whereas significant particle movement is visible for the frame at 136 μs. This indicates that a comparison between the results of this work can be made for these early times, but not for the later times where particle velocity relaxation is no longer negligible.

2.2. Representation of 2D-particle cloud

In the next section, spatial averaging will be used to reduce the 2-D simulation results to one dimension. In order to minimize the fluctuations in phase-averaged variables, a special configuration of particles is developed. Fig. 2 shows four different arrangements of particles: (a) a conventional square lattice, (b) a staggered lattice, (c) an inline distributed arrangement, and (d) the final proposed, more complex, arrangement. The diameter and number of particles are related to the area fraction via

$$\alpha_d = \frac{N\pi D_p^2}{4L^2}. \tag{1}$$

The particle diameter is based upon the cloud containing $N = 25$ particles such that the area fraction occupied by the particles is $\alpha_d = 0.15$. This gives a particle diameter $D_p = 0.089$. As shown in Fig. 2, the thickness of the particle curtain is $L = 1$ with the leading edge located at $x = -0.5$ and the trailing edge located at $x = 0.5$.

Fig. 3 shows the normalized cross-sectional area associated with each particle arrangement. At each x-location, this quantity is defined as the ratio of the open cross-section by the height of the particle cloud. The ideal normalized cross-sectional area is

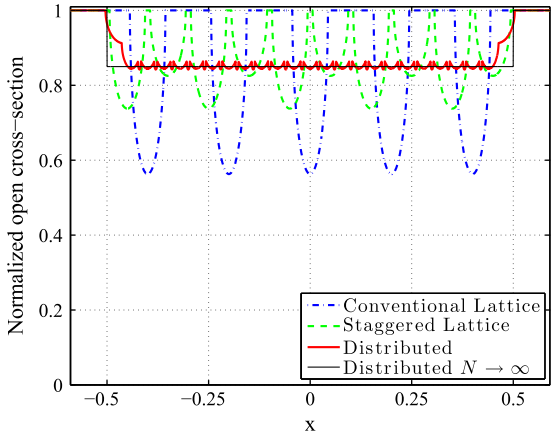

Fig. 3. Planar-averaged cross sections are plotted for conventional square, staggered, distributed, and an idealized distributed curve in the limit $N \to \infty$.

the continuous phase area fraction $\alpha_c = 1 - \alpha_d = 0.85$. In the conventional square lattice arrangement (Fig. 2(a)), the particles align in such a way that large variations in the cross-sectional area exist; the cross-section oscillates around the prescribed continuous phase volume/area fraction. As shown in Fig. 2(b), these oscillations can be reduced by considering a staggered lattice. However, the oscillations remain.

In order to minimize these oscillations and introduce the possibility for the oscillations to tend toward zero as the number of particles becomes large, the particles are distributed in the x-direction with equal spacing $\delta = L/N$. In this arrangement (Fig. 2(c)), each particle occupies a unique x-location, which minimizes the fluctuations in plane-integrated cross-section. The resulting

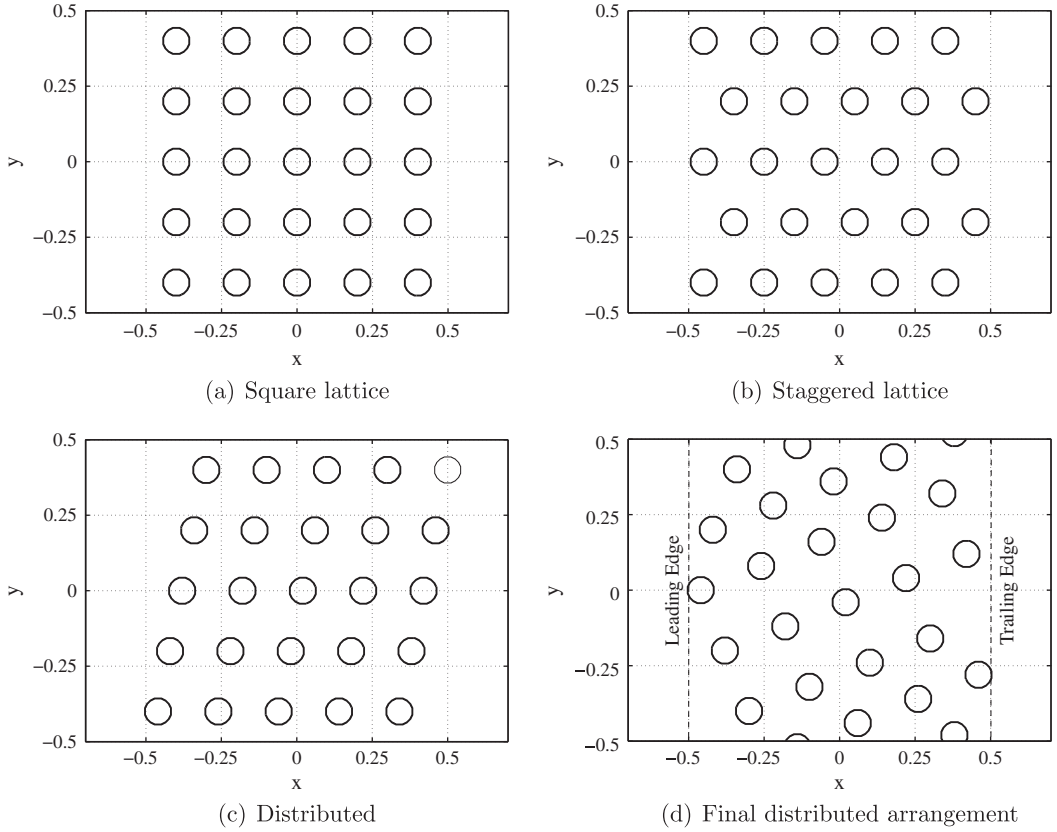

Fig. 2. Comparison between conventional square lattice, staggered lattice, and distributed lattice arrangements.

"distributed" arrangement limits the fluctuations in planar-averaged cross-section to less than 0.8%. This clear improvement comes from the fact that there are 25 unique x-locations in this new arrangement compared to only 5 for the conventional lattice and 10 for the staggered lattice.

The final arrangement shown in Fig. 2(d) shuffles some of particle rows from the inline distributed arrangement and shifts each consecutive column of particles in the positive y-direction by approximately one particle diameter. This modification gives the particle distribution a more random appearance. Since the x-locations are identical between arrangements (c) and (d), the normalized cross-sections (Fig. 3) are identical.

With the current non-dimensionalization, the width of the particle curtain is unity. A full discussion of the non-dimensionalization is presented in the next section. The cloud is located between $x = -0.5$ and 0.5, and the computational domain spans the range $x \in [-2.5, 3.5]$ and $y \in [-0.5, 0.5]$. In order to limit the particle curtain to $x \in [-0.5, 0.5]$, the 25th particle that lies on the cloud boundary (thin circle in Fig. 2(c)) is removed, which is why there are 24 particles in the distributed arrangements. Inflow and outflow conditions are used on the left and right boundaries, respectively, and the top and bottom boundaries are periodic to simulate an infinitely long cloud. The simulation uses a Cartesian grid. The grid spacing is uniform in the y-direction and in the x-direction for $x \in [-1.5, 1.5]$. In this region, the cells have unity aspect ratio, $\Delta x = \Delta y$. Outside of this range, unequal spacing (i.e. stretched mesh) is used in the x-direction.

Simulations were performed for four different levels of resolution to determine grid sensitivity. A list of the different levels of resolution and the equivalent number of points per particle diameter are listed in Table 1.

It should be reiterated that the two-dimensional configuration described above is not intended to provide a quantitatively accurate comparison with experimental data (Wagner et al., 2012). The current motivation is to capture qualitatively the physics of the shock-particle cloud interaction and use the volume-averaged solution to test the assumptions associated with the point-particle approach and 1-D volume-averaging.

2.3. 2-D equations

As stated earlier, the two-dimensional computations are conducted using the Euler equations. The particles are modeled as solid cylinder walls and discretized using a stair-step approach. Slip wall conditions are imposed on the cylinder walls in addition to the zero penetration condition. The nondimensional Euler equations are given by

$$\frac{\partial}{\partial t}\rho + \frac{\partial}{\partial x_i}\rho u_i = 0, \tag{2a}$$

$$\frac{\partial}{\partial t}\rho u_i + \frac{\partial}{\partial x_j}\rho u_i u_j + \frac{\partial}{\partial x_i} p = 0, \tag{2b}$$

$$\frac{\partial}{\partial t}\rho e_T + \frac{\partial}{\partial x_i}[u_i(\rho e_T + p)] = 0, \tag{2c}$$

Table 1
Four different levels of resolution were used for the 2-D simulations. Here, n_x and n_y are the number of cells in the x and y-directions, respectively.

Cells/D_p	n_x	n_y	Total cells
13	690	150	1.04E5
26	1241	300	3.72E5
52	2152	600	1.29E6
105	4062	1200	4.87E6

where the nondimensional quantities are defined with respect to the initial undisturbed dimensional gas state $[c_0', \rho_0']$ and a dimensional length scale L' defined as the thickness of the cloud. Primes are used to denote dimensional quantities. With this formulation, the nondimensional quantities are expressed in terms of dimensional quantities as $x = x'/L'$, $t = t'c_0'/L'$, $u = u'/c_0'$, $\rho = \rho'/\rho_0'$, $p = p'/\left(\rho_0' {c_0'}^2\right)$ and $e_T = e_T'/{c_0'}^2$.

The equation of state for a perfect gas is

$$p = (\gamma - 1)\rho e \tag{3}$$

$$= (\gamma - 1)\left(\rho e_T - \frac{1}{2}\rho u_i u_i\right), \tag{4}$$

where e is the internal energy, γ is the specific heat ratio, and the total energy e_T is defined

$$e_T = e + \frac{1}{2}u_i u_i. \tag{5}$$

For comparison with the experimental work of Wagner et al. (2012), the particle curtain depth L is approximated by the slit dimension $L = 3.2$ mm. The reference density $\rho_0' = 0.969$ kg/m^3 and sound speed $c_0' = 345$ m/s are determined from the undisturbed test section conditions.

2.4. Numerical method

The 2-D simulations are performed using a modified version of the NGA code (Desjardins et al., 2008). The Roe–Pike method (Roe and Pike, 1984) combined with MUSCL-Hancock data reconstruction (Toro, 1999) is used to solve the Euler equations (Eq. (2)). The van Leer limiter (van Leer, 1979) is used to minimize the effects of artificial viscosity/diffusion while maintaining a total variation diminishing solution. The method is first order accurate near shocks and contact discontinuities, and second order accurate elsewhere.

2.5. Initial conditions

The initial nondimensional Rankine–Hugoniot shock jump conditions for a $M = 1.67$ shock wave are

$$p_5 = 2.21 \qquad p_0 = 0.714, \tag{6a}$$

$$\rho_5 = 2.15 \qquad \rho_0 = 1, \tag{6b}$$

$$u_5 = 0.896 \qquad u_0 = 0, \tag{6c}$$

where subscript 5 denotes the fluid condition upstream of the incoming shock and subscript 0 indicates the undisturbed fluid downstream of the shock. The reason for this notation will be apparent shortly. The shock wave is initially located at the left domain boundary $x = -2.5$.

3. Numerical results

The first part of this section will focus on the effects of multiple dimensions. The second part defines the volume averaging procedure used to assess grid dependence and demonstrates the importance of unsteady velocity fluctuations on the volume-averaged equations.

3.1. General flow behavior

Fig. 4 shows snapshots of pressure (p/p_0) contours at several different instances after the shock first encounters the particle cloud. When the incident shock first hits the particle cloud, a reflected shock wave is created (Fig. 4(b)). The reflected shock wave is comprised of multiple shock reflections, one from each particle,

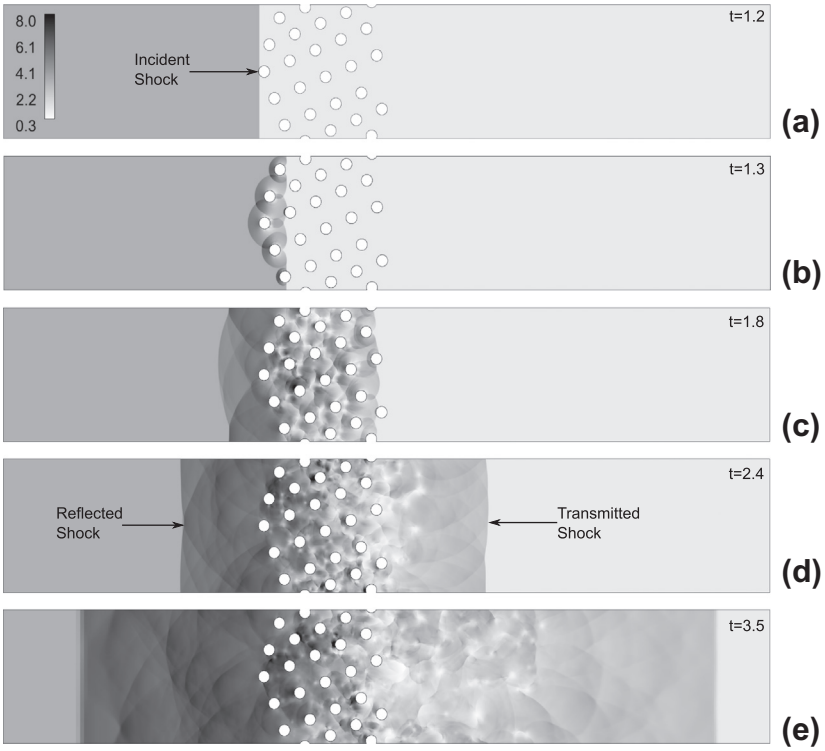

Fig. 4. A time series evolution of the normalized pressure (p/p_0) shows the reflected and transmitted shock waves, as well as unsteady flow conditions both inside and behind the cloud.

which cumulatively coalesce to form a nearly planar shock front. The initial reflected shock wave has a relatively small magnitude (Fig. 4(c)) in comparison to later times (Fig. 4(d)). As time proceeds, additional reflected waves from other particles within the cloud contribute to strengthening the amplitude of the reflected shock (Fig. 4(e)). Fig. 4 also shows a transmitted shock that traverses through the cloud and emerges into the undisturbed gas downstream.

The interaction of the shock wave with each cylinder in the current work is very similar to that characterized by Sun et al. (2005). When the incident shock wave impacts the cylinder, a regular reflection is formed. As the incident shock travels further along the cylinder, the regular reflection transitions to a Mach reflection. When the Mach reflections converge on the line of symmetry at the trailing edge of the cylinder, a region of high pressure is created, which subsequently expands and the pressure decreases.

Flow separation at the trailing edge of the cylinders is not observed until the transmitted shock wave has traveled approximately one diameter downstream of the cylinder. Shortly thereafter (about 0.01 time units), a recirculation zone forms behind each cylinder. The recirculation zone is initially symmetric, after which unsteady vortex shedding commences (Fig. 5). Although there is no physical viscosity present in the Euler equations, numerical viscosity is implicitly present. This numerical viscosity causes the initial flow separation to occur, and is discussed in detail in the next section.

The pressure behind the transmitted shock that initially emerges from the cloud has an average magnitude of $p/p_0 = 2.4$, which is 20% lower than that of the initial shock. This drop in pressure is due to the multiple shock reflections created from each particle interaction as the shock traverses the cloud. After the transmitted shock emerges from the cloud, the pressure at the trailing edge of the cloud continues to drop as unsteady wakes form behind each cylinder, which increases the drag and thereby further reduces the pressure.

Between the transmitted shock wave and the trailing edge of the cloud lies a region of fluid that is strongly unsteady and consists of vortices shed by each particle. Inside that region, localized pockets of low pressure exist in the vortex cores. This pressure may be as low as $p/p_0 = 0.3$, which is lower than the initial undisturbed gas condition. A quantified discussion of this region will be presented in Section 5.

The general behavior of the shock interaction with the particle cloud is best described using an x–t diagram. Fig. 6 shows a typical x–t diagram that is specific to the early interactions where the particles can be assumed to be frozen in place. Similar x–t diagrams

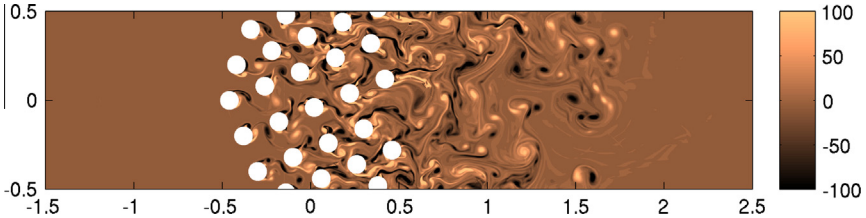

Fig. 5. Contour plot of vorticity at $t = 3.5$. As expected for flows with a Reynolds number near $Re = 2000$, unsteady vortices are shed from the surface of each cylinder.

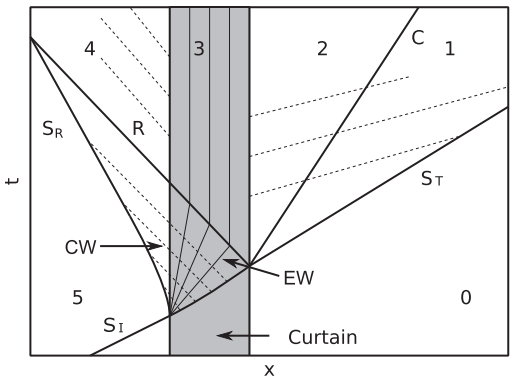

Fig. 6. An x–t diagram demonstrates the one-dimensional behavior observed in both the one- and two-dimensional model results. Six different regions are identified, which include the (0) undisturbed gas, (1) fluid behind the transmitted shock S_T, (2) fluid between the contact C and the cloud's trailing edge, (3) expansion across the cloud, (4) fluid behind the reflected shock, and (5) incident shock condition.

can be found in Rogue et al. (1998), Miura and Glass (1983), and Ling et al. (2012).

When the original shock impacts the leading edge of the cloud, a portion of it is transmitted (S_T) and part of it is reflected (S_R). An expansion fan moves through the cloud behind the transmitted shock S_T, which starts the formation of the pressure gradient across the cloud. When the transmitted shock emerges from the cloud's trailing edge, a contact C and a rarefaction wave R are created. The contact propagates downstream and separates region 1 and 2. The rarefaction wave stops the expansion fan's propagation and sets up a steady pressure gradient across the cloud (region 3). Additionally, when the rarefaction reaches the leading edge of the cloud, the pressure in region 4, which was gradually increasing from the cumulative addition of compression waves CW, becomes constant.

The steady-state pressure gradient inside the particle cloud does not form immediately after the rarefaction R passes back through the cloud. Instead, the pressure inside the cloud fluctuates about its mean value, emitting acoustic waves away from the cloud. These fluctuations are shown in Fig. 6 as dashed lines propagating away from the cloud (labeled CW) along the characteristic lines $u - c$ and $u + c$.

It is possible to make some qualitative comparisons with the experimental results at early times when the frozen particle assumption is reasonably accurate. The 35 μs frame in Fig. 1 shows reflected and transmitted shock waves, similar to the current results. The 35 μs frame also shows the presence of a contact wave between the trailing edge of the particle cloud and the transmitted shock. In general, the 2-D simulation contained in this work appears to reproduce the essential physics contained in the experiments.

3.2. Grid dependence

As a result of the large particle Reynolds number found in the experiment of Wagner et al. (2012) (near $Re = 2000$), the Euler equations (no molecular viscosity) have been used as a first approach to perform the 2-D numerical computations. It is important to note that it is theoretically impossible to obtain numerical convergence using an L_∞ norm with the Euler equations. Nevertheless, the numerical method implicitly contains numerical viscosity in order to capture shocks and contact discontinuities. Furthermore, the 2D-particles are discretized on a Cartesian mesh using a stair-stepped approach (i.e. the walls are not smooth). It is hence natural to wonder which quantities from the numerical results, if any, are grid dependent. Towards that goal, a grid dependence study is performed to determine the solution's sensitivity to numerical viscosity. Since numerical convergence cannot be obtained using an L_∞ norm with the Euler equations, planar-averaged quantities are used to gauge grid dependence.

2-D simulations were performed using 13, 26, 52, and 105 points per cylinder diameter. A full list of grid details can be found in Table 1. Fig. 7 shows the planar-averaged pressure at $t = 2.5$ for these different levels of resolution. While there are oscillations due to the finite number of grid points and 2D-particles, there is little noticeable difference in the mean values between the four different levels of resolution. Since the pressure drop through the particle cloud is due mainly to the drag around the 2D-particles, we can conclude that the particle drag is independent of any artificial viscosity. It is important to note that when the Reynolds number for an individual particle is in the range $10^3 < Re < 10^5$, known as the inertial range (Clift et al., 1978; Crowe et al., 2012), the drag coefficient is nearly independent of Reynolds number. Hence, the present results may be typical of flows in the inertial range $10^3 < Re < 10^5$.

While the numerical viscosity is not obviously equivalent to the true viscosity, the effective/observed particle boundary layer wakes contain many features expected in a real flow. Aside from the planar-averaged convergence, we caution that a full exposition of the detailed physics of the particle boundary layer and wakes awaits fully three-dimensional, viscous calculations, that will be the subject of future work.

3.3. Velocity fluctuations

Figs. 4 and 5 indicate that unsteady flow exists inside and behind the particle cloud. It is unclear how strong the unsteady flow is in comparison to the mean flow. Thus it is helpful to calculate the mean and RMS velocities. In order to make this comparison, volume average definitions must be made. The volume average of a quantity ϕ is defined as

$$\bar{\phi} = \frac{1}{V}\int_V \phi dV, \tag{7}$$

where V is the sampling volume including both the continuous and disperse phases. If the volume integral is limited to the continuous phase, the phase average (or Reynolds average) is defined

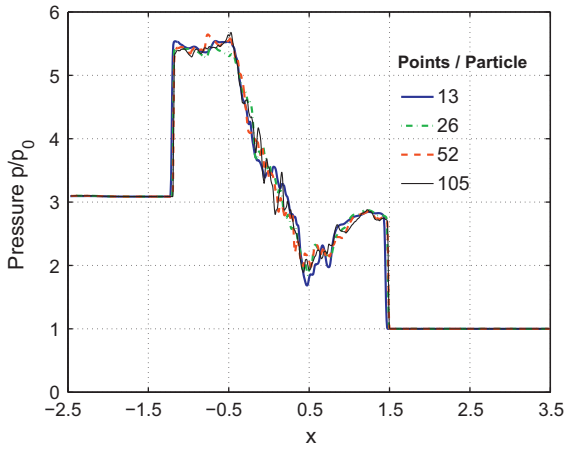

Fig. 7. The number of points required to resolve a single particle was varied by almost an order of magnitude. These planar-averaged pressure profiles at $t = 2.5$ indicate that the solution is independent of grid resolution.

$$\langle\phi\rangle = \frac{1}{V_c}\int_{V_c}\phi dV, \tag{8}$$

where V_c is the volume inside V that only includes the continuous phase, so that the Reynolds and volume averages are related by

$$\bar{\phi} = \alpha_c\langle\phi\rangle, \tag{9}$$

where $\alpha_c = 1 - \alpha_d$ is the continuous phase volume fraction. Finally, the mass average (Favre average) is defined as

$$\tilde{\phi} = \frac{\overline{\rho\phi}}{\bar{\rho}} = \frac{\langle\rho\phi\rangle}{\langle\rho\rangle}. \tag{10}$$

As mentioned earlier, in 2-D, the sampling volume becomes a sampling area. The phase-averaged quantity $\langle B\rangle(x)$ for a quantity $B(x,y)$ is obtained using Eq. (8), where V_c is a sampling area that is thin in the x-direction and spans the entire domain height in the y-direction. This equation is used to determine the phase-averaged quantities for the conserved variables ρ, ρu_i, and ρe_T at each x-position. The primitive variables $\tilde{u}_i$ and $\langle p\rangle$ are determined from these phase-averaged quantities.

With these definitions, the RMS velocity is defined

$$u_i'' = \sqrt{\widetilde{u_i^2} - \tilde{u}_i^2}. \tag{11}$$

Fig. 8 plots the Favre mean velocity in the x-direction $\tilde{u}$ and RMS velocities at $t = 3.5$. The mean velocity in the y-direction $\tilde{v}$ is zero, as can be anticipated, and is not plotted. As expected, the velocity fluctuations induced by acoustic waves are small. These regions exist upstream of the particle cloud $x < -0.5$ and just behind the transmitted shock before the large oscillations begin $x > 1.5$.

It is clear that inside and downstream of the particle cloud $-0.5 < x < 1.5$ the RMS fluctuation velocities are nearly equal to the mean flow velocity $\tilde{u}$. The RMS velocities are nearly identical for the first 75% of the particle cloud $-0.5 \leqslant x \leqslant 0.25$. In the last 25% of the cloud the streamwise RMS velocity u'' is appears higher than the transverse velocity v''. However, this could be due to statistical noise. With the exception of the last 25% of the particle cloud the flow could be considered isotropic.

If $u_i'' \approx \tilde{u}$, which is shown in Fig. 8, a substantial amount of energy is converted to turbulent kinetic energy. Behind the transmitted and reflected shock wave the turbulent kinetic energy contribution appears to be small. However, inside the particle cloud and immediately behind it (in the wake) it is clear that strong unsteady effects are present. In a point-particle model these effects are often neglected and must be modeled in order to capture accurately the entire flow behavior.

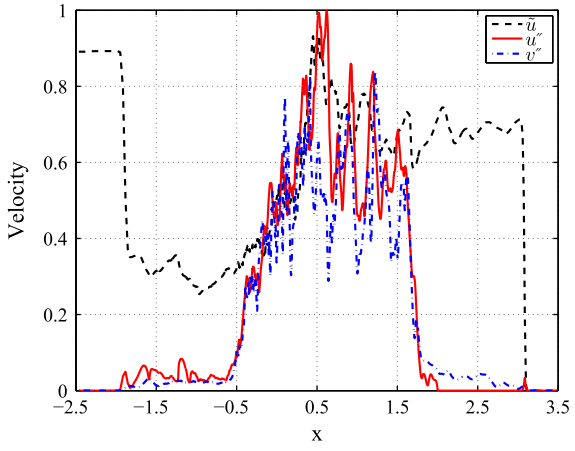

Fig. 8. The RMS velocities are plotted simultaneously with the mean flow velocity $\tilde{u}$ for $t = 3.5$. The RMS velocity and mean flow velocities $\tilde{u}$ are nearly equal inside and behind the curtain.

It is important to recall that wake fluctuations and vortical structures behind cylinders are known to be more intense than spheres. Thus, the observed fluctuations may appear stronger than what may be observed for a cloud of spherical particles with the same volume fraction.

4. Phase-averaged equations

A full derivation of the volume-averaged multiphase Navier–Stokes equations can be found in Crowe et al. (2012). The purpose here is to present the volume-averaged multiphase Navier–Stokes equations with all terms that are consistent with the 2-D simulation. Once again, mass and heat transfer between phases, as well as viscous stresses in the continuous phase are not considered. Since the 2D-particles are frozen the disperse phase equations are omitted.

4.1. Continuity

Given the definitions in Section 3.3, the volume-averaged variable density continuity equation from Crowe et al. (2012) for the continuous phase is

$$\frac{\partial}{\partial t}(\alpha_c\langle\rho\rangle) + \frac{\partial}{\partial x_i}(\alpha_c\langle\rho\rangle\tilde{u}_i) = 0. \tag{12}$$

No unclosed terms are created and an exact mapping exists between the volume-averaged quantities and the original continuity Eq. (2a).

4.2. Momentum

The variable density volume-averaged momentum equation for the continuous phase can be obtained from the Navier–Stokes equations and can be expressed as

$$\frac{\partial}{\partial t}(\alpha_c\langle\rho\rangle\tilde{u}_i) + \frac{\partial}{\partial x_j}(\alpha_c\langle\rho\rangle\tilde{u}_i\tilde{u}_j) = -\frac{\partial\langle p\rangle}{\partial x_i} - \frac{\partial}{\partial x_j}(\alpha_c\langle\rho u_i'' u_j''\rangle) - \frac{1}{V}\sum_k F_{k,i}, \tag{13}$$

where the viscous shear stresses, body forces, and mass sources have been neglected. This formulation is identical to that in Ling et al. (2011, 2012) for a similar model problem. The primary difference is the presence of the Reynolds stress term $\alpha_c\langle\rho u_i'' u_j''\rangle$. This term exists as a biproduct of the volume-averaging procedure (Crowe et al., 2012). It is common to neglect the Reynolds stress term for dilute flows (Miura and Glass, 1982, 1983; Miura, 1990). However, the large RMS velocities shown in Fig. 8 suggest that this term is of a similar magnitude to the mean convective flux $(\alpha_c\langle\rho\rangle\tilde{u}\tilde{u})$ and hence should not be neglected.

The last term on the right hand side of Eq. (13) is the force coupling term. This term represents the sum of all forces acting on the particles in the averaging volume V. These include the quasi-steady drag force, pressure gradient force, inviscid-unsteady (added-mass), and viscous-unsteady (Basset) forces (Magnaudet and Eames, 2000; Balachandar and Eaton, 2010; Crowe et al., 2012). The sum of all these forces on a single particle is

$$F_i = F_i^{\mathrm{qs}} + F_i^{\mathrm{pg}} + F_i^{\mathrm{am}} + F_i^{\mathrm{vu}}, \tag{14}$$

where particle rotation effects have been neglected. The four different forces are defined

$$F_i^{\mathrm{qs}} = \frac{1}{2}\rho_c C_D(Re^p, M^p, \alpha)A_p|u_i - u_i^p|(u_i - u_i^p), \tag{15}$$

$$F_i^{pg} = -V_p \frac{\partial p}{\partial x_i}, \tag{16}$$

$$F_i^{am} = C_a(M^p, \alpha) V_p \rho_c \left(\frac{Du_i}{Dt} - \frac{du_i^p}{dt} \right), \tag{17}$$

$$F_i^{vu} = 3D_p^2 \sqrt{\pi \rho_c \mu_c} \int_0^t K_{vu}(t-\chi, Re^p, M^p, \alpha) \frac{\frac{Du_i}{Dt} - \frac{du_i^p}{d\chi}}{\sqrt{t-t'}}, \tag{18}$$

where C_D is the quasi-steady drag coefficient, A_p the particle cross-section, u_i^p the particle velocity, V_p the particle volume, C_a the added-mass coefficient, D_p the particle diameter, μ_c the continuous phase viscosity, and K_{vu} is the viscous-unsteady force kernel. In the current analysis, the disperse phase velocity is zero. Furthermore, the flow is two-dimensional so the 2-D particle "cross-section" is its diameter D_p and the "volume" of a particle is its area, which for a circle is $A_p = \pi D_p^2/4$.

The forces in Eqs. (15)–(18) are well defined for dilute and incompressible flows. However, for dense or high speed flows, correction functions must be applied to account for these effects. These correction functions provide correlations for C_D, C_a, and K_{vu}. Although a considerable amount of literature exists for dense incompressible (Ergun, 1952; Gibilaro et al., 1985; Di Felice, 1994; Makkawi, 2003) and dilute high speed flow (Crowe et al., 2012; Hermsen, 1979), little information exists for dense, high speed flows. Furthermore, these correction functions have been developed for spherical particles. Since the objective of the current work is to model a cloud of 2-D cylinders, the correction functions established in the literature cannot be used.

The approach used in this work is to use a constant artificial quasi-steady drag coefficient that captures both the quasi-steady drag force and the effects of the added-mass and Basset forces. A full discussion on this assumption and the sensitivity of the solution results to the presence of other explicitly modeled forces can be found in the Appendix. It is shown that for this particular case, an effective constant drag coefficient can capture with reasonable accuracy the effects of these other forces. However, this effective drag coefficient should not be interpreted as a universal drag coefficient that may be applied to other situations.

4.3. Total energy

The volume-averaged total energy equation can derived for variable density flows in a manner similar to that outlined in Crowe et al. (2012). For clarity, we present a short summary of the derivation of the unclosed fluctuation terms. The volume-average of the total energy equation with variable density is written

$$\frac{\partial}{\partial t}\alpha_c\langle\rho\rangle\tilde{e}_T + \frac{\partial}{\partial x_j}\alpha_c\langle\rho\rangle\tilde{h}_T\tilde{u}_j = 0, \tag{19}$$

where the total energy and enthalpy flux are defined as

$$\langle\rho\rangle\tilde{e}_T = \langle\rho\rangle\tilde{e} + \frac{1}{2}\langle\rho\rangle\tilde{u}_i\tilde{u}_i + \frac{1}{2}\langle\rho u_i'' u_i''\rangle, \tag{20}$$

and

$$\langle\rho\rangle\tilde{h}_T\tilde{u}_j = \langle\rho\rangle\tilde{e}\tilde{u}_j + \frac{1}{2}\langle\rho\rangle\tilde{u}_i\tilde{u}_i\tilde{u}_j + \langle p\rangle\tilde{u}_j + \langle\rho\rangle\widetilde{u''\pi''} + \frac{1}{2}\tilde{u}_j\langle\rho u_i'' u_i''\rangle + \left\langle \rho u_j'' e'' \right\rangle, \tag{21}$$

$$+ \tilde{u}_i\left\langle \rho u_j'' u_i'' \right\rangle + \frac{1}{2}\left\langle \rho u_j'' u_i'' u_i'' \right\rangle, \tag{22}$$

where $\pi'' = (p/\rho)''$. The pressure velocity terms are obtained through the following procedure

$$\overline{u_j p} = \overline{\rho u_j \left(\frac{p}{\rho}\right)} = \overline{\rho(\tilde{u}_j + u_j'')\left[\widetilde{\left(\frac{p}{\rho}\right)} + \pi''\right]} = \bar{p}\tilde{u}_j + \overline{\rho u_j'' \pi''}$$
$$= \alpha_c\langle p\rangle\tilde{u}_j + \alpha_c\langle\rho\rangle\widetilde{u_j''\pi''}. \tag{23}$$

Clearly, the energy equation contains many more unclosed terms than the momentum equation.

The total energy $\langle\rho\rangle\tilde{e}_T$ is comprised of the phased-averaged total energy $\langle\rho\rangle\tilde{e} + \langle\rho\rangle\tilde{u}_i\tilde{u}_i/2$ and the turbulent kinetic energy $k_c = \langle\rho u_i'' u_i''\rangle/2$. Fig. 9 compares the volume-averaged internal energy $\langle\rho\rangle\tilde{e}$, kinetic energy $\langle\rho\rangle\tilde{u}\tilde{u}/2$, and turbulent kinetic energy k_c for the 2-D simulation at $t = 3.5$. The kinetic energy $\langle\rho\rangle\tilde{u}\tilde{u}/2$ is consistently an order of magnitude lower than the internal energy for the entire domain. For higher speed shock waves the kinetic energy could be equal to or even greater than the internal energy. Inside the particle cloud and downstream inside the wake the kinetic energy $\langle\rho\rangle\tilde{u}\tilde{u}/2$ is equal in magnitude to the turbulent kinetic energy k_c. Outside of this region the turbulent kinetic energy is two orders of magnitude smaller.

4.4. 1-D volume-averaged model

A volume-averaged model will be used to investigate the validity of the point-particle approach in modeling a shock wave impacting a dense non-compacted cloud of 2D-particles. Since the 2-D configuration in Section 2.2 is periodic in the transverse direction, the volume-averaged equations (Eqs. (12), (13) and (19)) can be reduced easily to one dimension. When the 2D-particles are frozen in place, the particle velocity is zero and the volume fraction is a function of position only $\alpha = \alpha(x)$. Thus, the 1-D volume averaged equations become

$$\frac{\partial}{\partial t}(\alpha_c\langle\rho\rangle) + \frac{\partial}{\partial x}(\alpha_c\langle\rho\rangle\tilde{u}) = 0, \tag{24a}$$

$$\frac{\partial}{\partial t}(\alpha_c\langle\rho\rangle\tilde{u}) + \frac{\partial}{\partial x}[\alpha_c(\langle\rho\rangle\tilde{u}^2 + \langle p\rangle)] = \langle p\rangle\frac{\partial\alpha_c}{\partial x} - \frac{2}{\pi D_p}C_D\alpha_d\langle\rho\rangle|\tilde{u}|\tilde{u}, \tag{24b}$$

$$\frac{\partial}{\partial t}(\alpha_c\langle\rho\rangle\tilde{e}_T) + \frac{\partial}{\partial x}(\alpha_c\langle\rho\rangle\tilde{u}\tilde{h}_T) = 0, \tag{24c}$$

where C_D is an artificial effective drag coefficient. The total energy and enthalpy are defined

$$\langle\rho\rangle\tilde{e}_T = \langle\rho\rangle\tilde{e} + \frac{1}{2}\langle\rho\rangle\tilde{u}^2, \tag{25}$$

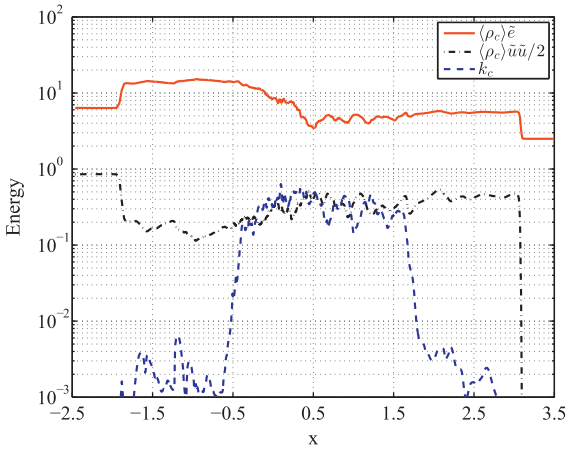

Fig. 9. The phase-averaged internal and kinetic energies are plotted simultaneously with the turbulent kinetic energy k_c for $t = 3.5$.

$$\langle\rho\rangle\tilde{h}_T = \langle\rho\rangle\tilde{e} + \frac{1}{2}\langle\rho\rangle\tilde{u}^2 + \langle p\rangle. \quad (26)$$

Neglecting the unclosed terms is a standard approach used to model shock waves impacting a dilute particle cloud (Miura and Glass, 1982, 1983; Miura, 1990). This assumption is often valid for sufficiently dilute flows. However, this approach was also recently used to model a shock wave impacting a dense particle cloud (Ling et al., 2012) with similar conditions as in this work. The results presented here demonstrate that since the Reynolds stress and static pressure are equal in magnitude, it is anticipated that the 1-D model results will deviate substantially from the 2-D results inside the unsteady region.

5. Model comparison

One of the primary objectives of this work is to isolate the momentum coupling between the two phases and assess the importance of the Reynolds stress. Eqs. (24) are used to model the 2-D problem in 1-D using a volume-averaged model.

5.1. One-dimensional domain

The continuous phase volume fraction α_c in the one-dimensional model is constructed to reflect accurately the phase-average volume fraction in the 2-D simulation. Fig. 10 compares the 1-D disperse phase volume fraction with the exact volume-averaged disperse phase volume fraction computed from the 2-D simulation with averaging width of $D_p/2$.

The computational domain is in the range $x \in [-4, 6]$ with a total of 400 points across the domain. As for the 2-D simulations, the particle cloud is located $x \in [-0.5, 0.5]$ and the particle diameter is $D_p = 0.089$. The initial flow conditions are defined in Section 2.5.

Eqs. (24) are solved using the compressible flow solver developed for the dynamically Adaptive Wavelet-Collocation Method (AWCM) (Regele and Vasilyev, 2009). To assess the sensitivity of the results to the grid resolution, the grid was increased by up to 8 times with a total of 3200 points. The solution results remained unaffected, with the exception of the reflected and transmitted shock thicknesses. This is expected because the numerical scheme is near first order accurate at these locations.

5.2. Drag coefficient

As discussed in Section 4.2 and in the Appendix, the drag coefficient C_D in Eq. (24b) is understood to be an artificial effective drag coefficient that embodies the quasi-steady, added mass, and Basset forces. This drag coefficient is a function of the particle shape, Reynolds number Re, Mach number M, and volume fraction α_c. It is an unknown parameter in the 1-D model. The effective drag coefficient C_D is determined by finding the value that matches best the reflected and transmitted shock locations and magnitudes.

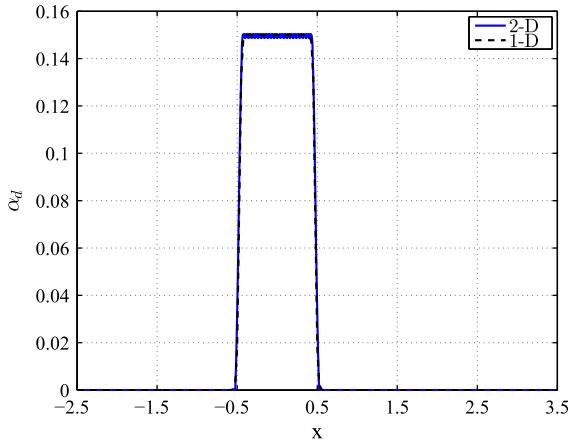

Fig. 10. Disperse phase volume fraction for the 1-D model compared with the exact volume-averaged volume fraction from the 2-D simulation.

The effective drag coefficient that most accurately captures the transmitted and reflected shock wave positions and magnitudes was found to be $C_D = 3.3$. Fig. 11 compares the average density and velocity profiles for both the exact 2-D results and 1-D model results at $t = 3.5$. It is interesting to note that both the reflected and transmitted shock positions are nearly identical, between the 1-D and 2-D results. Additionally, the 2-D results appear to oscillate around the 1-D model results for a significant portion of the solution.

Fig. 11 shows the density and velocity profiles for two additional cases where the drag coefficient is increased and decreased by 30%. Small, yet noticeable, differences can be observed in the shock locations as well as in the magnitude of the pressure behind the shocks. This suggests that the methodology is adequate to evaluate an effective drag coefficient and that it is reasonable to use two significant figures for the value.

5.3. 2-D and 1-D comparison

Figs. 12–14 compare x–t diagrams for the density, velocity, and pressure, respectively. Both the 1-D model and 2-D results show the basic flow behavior described in the x–t diagram (Fig. 6) of the previous section. In the density diagram (Fig. 12), both results show the reflected (S_R) and transmitted (S_T) shocks after the incident shock S_I first impacts the particle cloud. The expansion across the cloud is captured both during its formation and after it has formed a steady-state expansion. The existence of the contact C is consistent between both sets of results, and the density magnitude and slope are similar as well. However, the observed contact does not appear as a traditional contact discontinuity. While it does propagate at the local fluid velocity, the density difference is separated by a region of finite thickness.

The velocity in Fig. 13 is similar. Although the velocity contour shows some unsteadiness primarily behind the cloud, Fig. 11(b) indicates that at $t = 3.5$ the 2-D exact solution oscillates about the 1-D model solution.

In Fig. 14, the 2-D x–t diagram shows the presence of coherent compression waves propagating in both the $-x$ and $+x$-directions away from the cloud region. These waves are absent in the 1-D model. Inside the cloud of the 2-D simulation, it is difficult to trace the characteristic lines, which suggests that the compression waves originate from the cloud itself. This is consistent with the observation of coherent localized compression waves in the 2-D pressure contour plot in Fig. 4. These waves appear to be repeated internal reflection/transmission waves created by the initial shock that continue to reverberate inside the cloud.

Pressure is normally constant across a true contact discontinuity. In the 1-D model, this is shown to be true (see Fig. 14(a) for $x > 0.5$). In the 2-D simulation, the contact separates a region of predominantly steady flow (only disturbed by weak periodic acoustic waves), and a region of unsteady flow with large oscillating pressure disturbances associated with vortex shedding. A quantified analysis of these results is presented in the next section.

5.4. Quantified reynolds stress differences

Fig. 15 compares the pressure at $t = 3.5$ for the 1-D model and exact 2-D results. The average pressure in the 2-D result is consistently lower than that predicted by the 1-D model inside the particle cloud and downstream of the trailing edge until $x \approx 1.5$. As

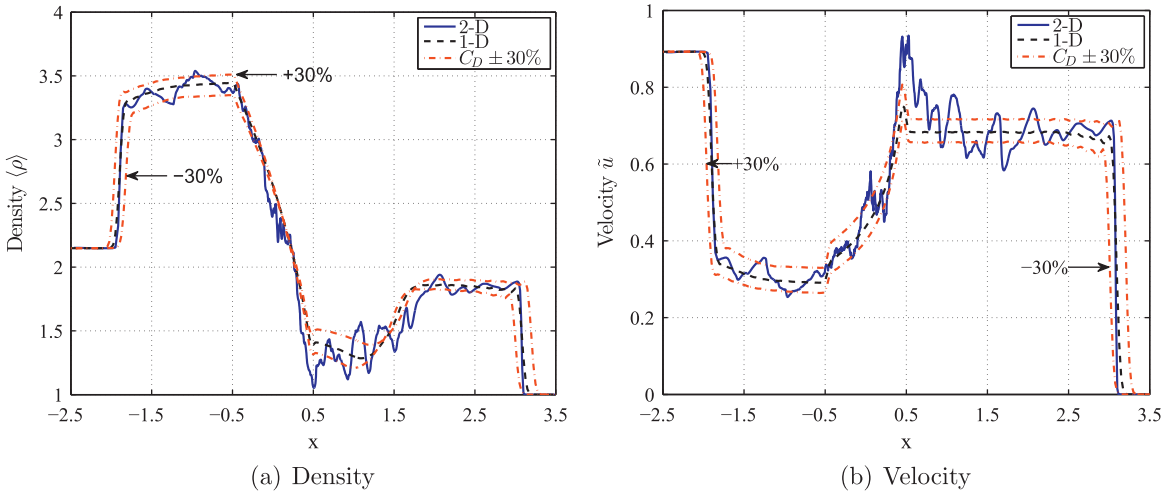

Fig. 11. A comparison between the 1-D model and 2-D phase-averaged solutions at $t = 3.5$ indicates that the density and x-velocity of the 2-D phase-averaged solution oscillates around the one-dimensional model solution. Two additional 1-D simulations were performed with the drag coefficient increased/decreased by 30%.

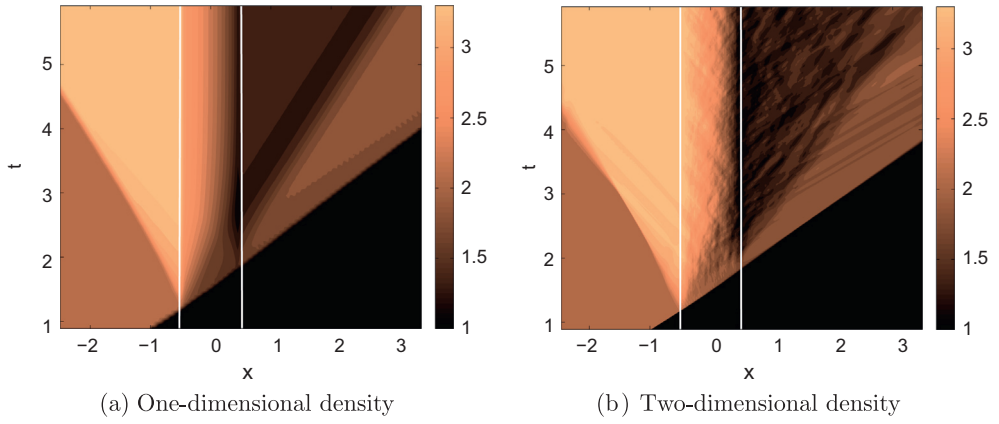

Fig. 12. x–t diagrams for density $\langle\rho\rangle$ compare the (a) one-dimensional and (b) two-dimensional planar average solutions.

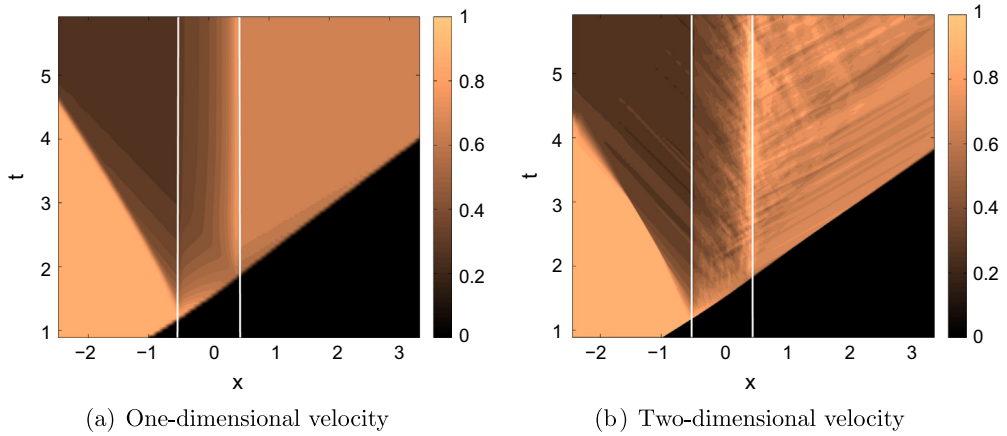

Fig. 13. x–t diagrams for velocity $\tilde{u}$ compare the (a) one-dimensional and (b) two-dimensional planar average solutions.

mentioned earlier, this is attributed to the fluctuations associated with vortical structures, which is a behavior that the 1-D model, in its current form, is incapable of reproducing. Since the unsteady flow features travel downstream at the mean fluid velocity, the contact discontinuity marks the transition between a smooth transmitted shock region and an unsteady wake region.

Unlike the continuity equation, the volume-averaged momentum equation (Eq. (24b)) contains one unclosed Reynolds stress term (Drew and Passman, 1999). It is convenient to define a total pressure p_T to be the sum of the volume-averaged pressure $\langle p\rangle$ and the Reynolds stress

$$p_T = \langle p\rangle + \alpha_c\langle\rho u'' u''\rangle. \tag{27}$$

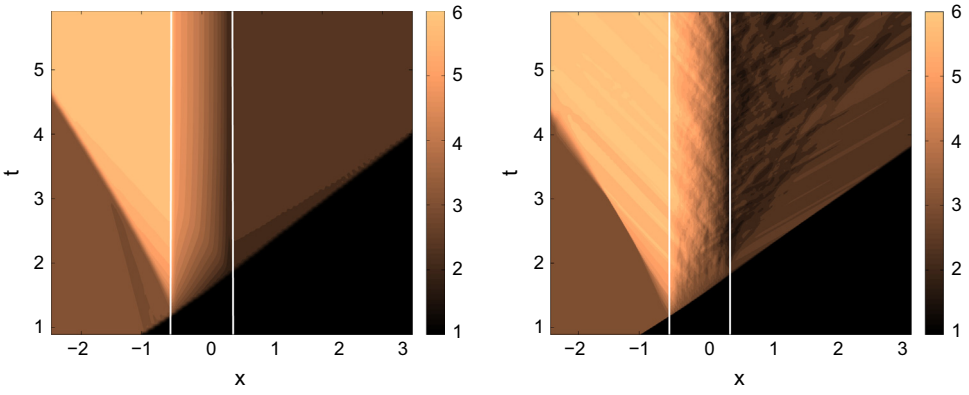

(a) One-dimensional pressure (b) Two-dimensional pressure

Fig. 14. x–t diagrams for pressure $\langle p \rangle$ compare the (a) one-dimensional and (b) two-dimensional planar average solutions. The contact discontinuity at $x = 1.5$ marks the interface between turbulent and non-turbulent regions.

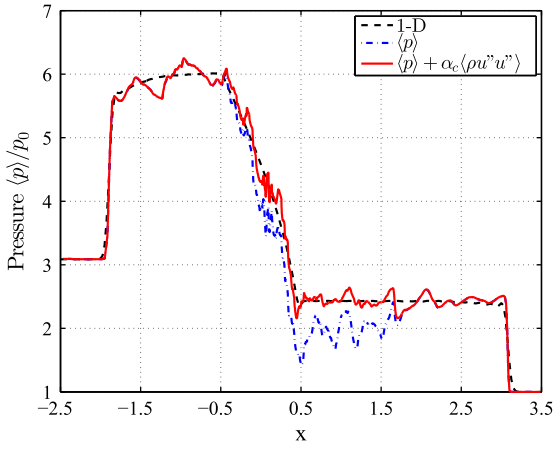

Fig. 15. At $t = 3.5$, the 2-D planar averaged solution is lower than the 1-D model between the cloud's trailing edge and the contact discontinuity.

Fig. 15 shows the 1-D and 2-D averaged pressures $\langle p \rangle$, as well as the total pressure p_T. The addition of the unclosed fluctuation Reynolds stress term accounts for the difference between the solutions. The 2-D $\langle p \rangle$ and p_T quantities are identical outside of the cloud and the unsteady fluctuation region, but only the total pressure matches accurately the 1-D model solution inside the cloud and unsteady region. The 1-D model overestimates the static pressure by including the energy that should be contained in turbulent kinetic energy. This implies that the pressure gradient in the 1-D model is not as steep as it should be and the effective drag coefficient contains elements of the pressure gradient force. Thus, the drag coefficient becomes ill-defined as it is not distinguishable completely from the pressure gradient force. Models must be developed to capture these unsteady effects so that these distinctions are maintained.

Additional simulations with different particle arrangements and different volume fractions would be necessary to develop proper closure models. However, such a study is beyond the scope of the present work.

5.5. Comparison summary

Based on the comparison of the results obtained with the 1-D volume-averaged model and the exact solution of the 2-D problem, it is possible to draw conclusions on the applicability of a volume-averaged model to capture a dense multiphase flow. First, Eqs. (24) use a constant artificial effective drag coefficient, which is found sufficient to capture the general flow physics, including transmitted and reflected shock waves, and the expansion within the particle cloud. Explicit inclusion of inviscid-unsteady (added-mass) and viscous-unsteady (Basset) forces will likely improve the model's ability to capture the fine details of the initial shock wave interaction. Despite the overall benefits listed previously, in its current form, the volume-averaged model is incapable of capturing the strong unsteady flow generated inside the cloud and its propagation downstream. Nevertheless, the present results suggest that very good comparison between 1-D model and 2-D results may be obtained with the consideration of a single additional term: the Reynolds stress term. Future work should focus on developing a model for this unclosed term.

6. Conclusions

In this work, the interactions between a shock wave and a dense non-compacted cloud of disperse phase 2D-particles is investigated. The focus is on 2D-particles of high inertia such that they can be considered frozen in place. In order to isolate the impact of modeling assumptions in volume-averaged point-particle models, momentum coupling is the only coupling term considered between phases. Multidimensional effects are demonstrated by modeling the disperse phase as fixed, solid, 2-D cylinders. The 2-D simulation demonstrates the importance of multidimensional effects and that the implications of these results are relevant to three dimensions.

The 2-D results show reflected and transmitted shock waves as well as an expansion wave across the particle cloud. A contact is formed at the cloud's trailing edge when the transmitted shock emerges from the cloud. However, this contact has a finite width and does not appear to be a true contact discontinuity in the conventional sense.

The 2-D simulation results exhibit strong unsteady effects. It is shown that inside the particle cloud and in the trailing wake the magnitude of the unclosed Reynolds stress term in the momentum equation is not negligible compared to the static pressure. Additionally, the turbulent kinetic energy in this region is equal in magnitude to the streamwise kinetic energy.

Commonly used, volume-averaged point-particle models often neglect unclosed terms such as the Reynolds stress. This assumption is not justified for the dense non-compacted regime. It is possible to match the transmitted and reflected shock wave locations by modifying the drag coefficient, but the pressure gradient inside and downstream of the particle cloud is captured incorrectly. This

approach creates drag coefficients that include aspects of the pressure gradient force, which muddles the distinction between the two forces.

A total pressure is demonstrated to account for the discrepancy between the 1-D model and the 2-D solution. The total pressure defined in this work may be useful to link other single particle drag correlations. In order to use the volume-averaged approach for dense high speed flows, models are needed for the unclosed Reynolds stress and turbulent kinetic energy terms.

Appendix A

The momentum coupling forces between phases are listed in Eqs. (15)–(18). These consist of the quasi-steady drag, the pressure gradient, inviscid-unsteady (added-mass), and the viscous-unsteady (Basset) forces. The analytical form of the pressure gradient force is known regardless of the density of the dispersed phase and the compressibility of the continuous phase. The other three forces involve correlation coefficients, namely the quasi-steady drag coefficient $C_D(Re^p, M^p, \alpha)$, the added-mass coefficient $C_a(M^p, \alpha)$, and the viscous-unsteady kernel $K_{vu}(t, Re^p, M^p, \alpha)$. These coefficients depend upon the particle Reynolds number Re^p, the particle Mach number M^p, the volume fraction α, and time t. Since the objective is to obtain a volume-averaged model that captures the basic flow behavior of the 2-D simulation, assumptions about the dependence of these coefficients on these parameters can be inferred from the solution results in order to reduce this large parameter space down to a more tractable problem.

First of all, Fig. 7 shows that the planar-averaged pressure profiles are independent of resolution, which also makes the solution independent of artificial viscosity. This implies that the flow is reminiscent of flow within the inertial range where the drag coefficient may be constant. The second approximation is to ignore the functional dependence on volume fraction. The third approximation revolves around the particle Mach number M^p. Analysis of the 2-D phase-averaged Mach number shows that the Mach number is constant through most of the particle cloud except during the initial passage of the shock wave. Finally, there is a temporal dependence in the Basset force. In the limit of constant acceleration and for long times $ct/D_p \gg 1$, the integral reduces to a constant times the acceleration $F^{vu} = C' Du/Dt$ (Parmar et al., 2008). This assumption is not valid during the early interactions where a clear history dependence should be included. This acceleration Du/Dt can be written in terms of the pressure gradient (Ling et al., 2012).

This suggests that to first order, there are essentially two types of forces involved in the flow, quasi-steady drag and pressure-gradient based forces. In this work, only the quasi-steady drag force is used to couple the two phases. It is found that an effective, yet artificial drag coefficient can be used to match the reflected and transmitted shock locations and magnitudes. It is unclear how contributions from these other unsteady forces may alter the flow behavior. Thus, additional simulations were performed with the added-mass force included explicitly in order to determine the solution sensitivity to these other forces.

The average Mach number inside the particle cloud is approximately $M \approx 0.4$. Irrespective of particle spacing effects, the added-mass coefficient of a cylinder for this Mach number is approximately $C_a = 2$ (Parmar et al., 2008). As described previously in Section 5.2, the quasi-steady drag coefficient is again calculated by performing multiple simulations with different quasi-steady drag coefficients until the reflected and transmitted shock waves match the 2-D phase-averaged solution. The obtained drag coefficient is $C_D = 1.8$, which is significantly smaller than the value $C_D = 3.3$ used without the added-mass force included. Fig. 16 shows the flow velocity for the 2-D phase-averaged solution, the 1-D phase-averaged model with only the quasi-steady drag and pressure gradient, and a final simulation with the added mass. The largest differences exist at the trailing edge of the cloud, which can be expected since changes in Mach number are significant in that region. Overall, the differences between the two volume-averaged models are small. Thus, only the quasi-steady drag coefficient $C_D = 3.3$ is used for the simulations contained in the main body of the paper.

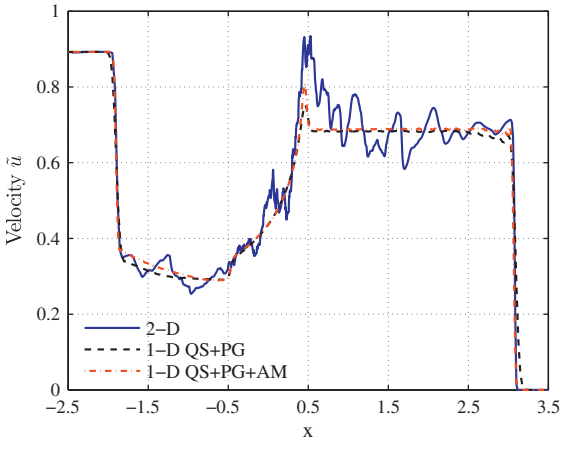

Fig. 16. Comparison between the 2-D phase-averaged solution, the 1-D model with quasi-steady drag and pressure gradient forces, and an additional 1-D model that includes the added-mass force.

References

Baer, M.R., Nunziato, J.W., 1986. A two-phase mixture theory for the deflagration-to-detonation transition (DDT) in reactive granular materials. Int. J. Multiphase Flow 12, 861–889.
Balachandar, S., Eaton, J.K., 2010. Turbulent dispersed multiphase flow. Annu. Rev. Fluid Mech. 42, 111–133.
Carrier, G., 1958. Shock waves in a dusty gas. J. Fluid Mech., 376–382.
Clemins, A., 1988. Representation of two-phase flows by volume averaging. Int. J. Multiphase Flow 14, 81–90.
Clift, R., Grace, J.R., Weber, M.E., 1978. Bubbles, Drops, and Particles. Academic Press.
Crowe, C.T., Schwarzkopf, J.D., Sommerfeld, M., Tsuji, Y., 2012. Multiphase Flows with Droplets and Particles, second ed. CRC Press.
Desjardins, O., Blanquart, G., Balarac, G., Pitsch, H., 2008. High order conservative finite difference scheme for variable density low Mach number turbulent flows. J. Comput. Phys. 227, 7125–7159.
Di Felice, R., 1994. The voidage function for fluid-particle interaction systems. Int. J. Multiphase Flow 20, 153–159.
Drew, D.A., 1983. Mathematical modeling of two-phase flow. Annu. Rev. Fluid Mech. 15, 261–291.
Drew, D.A., Passman, S.L., 1999. Theory of multicomponent fluids. Appl. Math. Sci. 135.
Ergun, S., 1952. Fluid flow through packed columns. Chem. Eng. Prog. 48, 89.
Gibilaro, L.G., Di Felice, R., Waldram, S.P., Foscolo, P.U., 1985. Generalized friction factor and drag coefficient correlations for fluid-particle interactions. Chem. Eng. Sci. 40, 1817–1823.
Hermsen, R.W., 1979. Review of particle drag models. In: JANAF Performance Standardization Subcommittee 12th Meeting Minutes, CPIA.
Ling, Y., Haselbacher, A., Balachandar, S., 2011. Importance of unsteady contributions to force and heating for particles in compressible flows. Int. J. Multiphase Flow 37, 1026–1044.
Ling, Y., Wagner, J.L., Beresh, S.J., Kearney, S.P., Balachandar, S., 2012. Interaction of a planar shock wave with a dense particle curtain: modeling and experiments. Phys. Fluids 24.
Magnaudet, J., Eames, I., 2000. The motion of high-Reynolds-number bubbles in inhomogeneous flows. Ann. Rev. Fluid Mech. 32, 659–708.
Makkawi, Y., 2003. The voidage function and effective drag force for fluidized beds. Chem. Eng. Sci. 58, 2035–2051.
Miura, H., 1990. Decay of shock waves in a dusty-gas shock tube. Fluid Dynam. Res. 6, 251–259.
Miura, H., Glass, I.I., 1982. On a dusty-gas shock tube. Proc. Roy. Soc. A: Math. Phys. Eng. Sci. 382, 373–388.

Miura, H., Glass, I.I., 1983. On the passage of a shock wave through a dusty-gas layer. Proc. Roy. Soc. A: Math. Phys. Eng. Sci. 385, 85–105.
Parmar, M., Haselbacher, A., Balachandar, S., 2008. On the unsteady inviscid force on cylinders and spheres in subcritical compressible flow. Philos. Trans. Ser. A, Math. Phys. Eng. Sci. 366, 2161–2175.
Parmar, M., Haselbacher, A., Balachandar, S., 2010. Improved drag correlation for spheres and application to shock-tube experiments. AIAA J. 48, 1273–1276.
Powers, J.M., Stewart, D.S., Krier, H., 1990. Theory of two-phase detonation-Part I: modeling. Combust. Flame 80, 264–279.
Regele, J.D., Vasilyev, O.V., 2009. An adaptive wavelet-collocation method for shock computations. Int. J. Comput. Fluid Dynam. 23, 503–518.
Roe, P.L., Pike, J., 1984. Efficient construction and utilisation of approximate Riemann solutions. In: Computing methods in applied sciences and engineering, vol. VI. pp. 499–518.
Rogue, X., Rodriguez, G., Haas, J., Saurel, R., 1998. Experimental and numerical investigation of the shock-induced fluidization of a particles bed. Shock Waves 8, 29–45.
Saito, T., 2002. Numerical analysis of dusty-gas flows. J. Comput. Phys. 176, 129–144.
Sangani, a.S., Zhang, D.Z., Prosperetti, A., 1991. The added mass, Basset, and viscous drag coefficients in nondilute bubbly liquids undergoing small-amplitude oscillatory motion. Phys. Fluids A: Fluid Dynam. 3, 2955.
Sun, M., Saito, T., Takayama, K., Tanno, H., 2005. Unsteady drag on a sphere by shock wave loading. Shock Waves 14, 3–9.
Toro, E.F., 1999. Riemann Solvers and Numerical Methods for Fluid Dynamics, second ed. Springer.
van Leer, B., 1979. Towards the ultimate conservative difference scheme. V. A second-order sequel to Godunov's method. J. Comput. Phys. 32, 101–136.
Wagner, J.L., Beresh, S.J., Kearney, S.P., Trott, W.M., Castaneda, J.N., Pruett, B.O.M., Baer, M.R., 2011. Interaction of a planar shock with a dense field of particles in a multiphase shock tube. In: Proc. 49th AIAA Aerospace Sciences Meeting, vol. 188. pp. 1–13.
Wagner, J.L., Beresh, S.J., Kearney, S.P., Trott, W.M., Castaneda, J.N., Pruett, B.O., Baer, M.R., 2012. A multiphase shock tube for shock wave interactions with dense particle fields. Exp. Fluids 52, 1507–1517.
Zhang, F., Frost, D., Thibault, P., Murray, S., 2001. Explosive dispersal of solid particles. Shock Waves 10, 431–443.